Validation of the synthetic model for the imaging heavy ion beam probe at the ASDEX Upgrade tokamak

P. Oyola,[1, a)] G. Birkenmeier,[2, 3] H. Lindl,[2, 3] J. Galdon-Quiroga,[1] J. Rueda-Rueda,[1] E. Viezzer,[1] A. Rodriguez-Gonzalez,[1] J. Hidalgo-Salaverri,[4] M. Garcia-Munoz,[1] B. Tal,[3] G. Anda,[5] J. Kalis,[2, 3] T. Lunt,[3] D. Refy,[5] M. Videla-Trevin,[1] and ASDEX Upgrade team[b)]

[1)] *Department of Atomic, Molecular and Nuclear Physics, Universidad de Sevilla*

[2)] *TUM School of Natural Sciences, Physics Department, Technical University of Munich, 85748 Garching, Germany*

[3)] *Max Planck Institute for Plasma Physics, 85748 Garching, Germany*

[4)] *Department of Mechanical Engineering and Manufacturing, Universidad de Sevilla*

[5)] *Centre of Energy Research, Budapest, Hungary*

(Dated: 10 July 2024)

Recent experiments at the ASDEX Upgrade tokamak have provided the first ever measurements from the imaging Heavy-Ion Beam Probe (i-HIBP). In this work, we show that the developed simulation framework can reproduce qualitatively the measurement's observed shape and position. Quantitatively we demonstrate that the model reproduces, within the experimental uncertainties, the observed signal levels. A detailed explanation of the synthetic model is presented, along with the calibration of the optical setup that reproduces the measurements.

Keywords: Plasma diagnostics, tokamak, beam probe, scintillators, density measurements, synthetic diagnostic

I. INTRODUCTION

The characteristics of the plasma edge in magnetically confined fusion plasmas play a fundamental role for the confinement performance, the impurity control and the heat exhaust capability of the chosen fusion plasma scenario[1]. Measurements of the plasma edge are important to identify the underlying physics of the phenomena taking place, as they strongly determine the plasma properties. Accurate measurements of the edge current density and density fluctuations are also crucial for the validation of models and numerical tools, which are necessary to develop predictive capabilities for a future fusion reactor scenario. A new diagnostic, the imaging Heavy Ion Beam Probe (i-HIBP)[2–6] has been installed and commissioned at the ASDEX Upgrade tokamak (AUG). It aims to provide simultaneous measurements of the edge current density and density fluctuations. This diagnostic shares properties with the traditional HIBP[7–9], based on the determination of plasma quantities by the analysis of a probing ion beam. For the HIBP, singly ionized heavy alkali ions, like cesium, are accelerated up to energies of the order of $\sim 1\,\mathrm{MeV}$ and then injected into the plasma. Due to its large gyroradius, the heavy ion reaches the plasma core and then escapes the plasma, where it impinges into a Faraday cup array or an energy analyzer. Traditional HIBPs have provided, both in tokamaks and stellarators, useful measurements of a wide range of phenomena ranging from equilibrium, profiles and electrostatic potential to turbulence and instabilities[10–12]. Two main differences can be highlighted between these diagnostics: the i-HIBP uses a neutral beam as a primary and the use of a scintillator as the active detector of the signal. As the beam is neutral, it will not get deflected by the magnetic field and can penetrate into the plasma following a linear path. This change allows the injection energies to be decreased down to about $50 - 100$ keV, reducing consequently the size of injector and high voltage components. The neutral beam ionizes as it reaches the plasma, mostly around the separatrix, and generates a set of singly ionized alkali ions along the injection path, as shown in the Fig. 1(a). These ions, the so-called secondary beam ions, will start a gyromotion, with a typical gyroradius of $\sim 20\,\mathrm{cm}$ at the AUG tokamak, until they escape the plasma and hit a scintillator plate, TG-Green[13] for the AUG setup, located in the limiter shadow. The light emitted by the scintillator is collected by a set of lenses and a fiber bundle and then transmitted outside the vacuum vessel to a camera. Changes in the electromagnetic field impact the particle orbits: magnetic field perturbations, δB_{pol}, shift the scintillator pattern globale, while perturbations in the electrostatic potential, $\delta\phi_{\mathrm{ES}}$, lead to smaller and local deflection on the scintillator pattern[2]. Changes in the plasma density and temperature impact the number of ions that reach the scintillator, thus, determining the light level detected with the camera. A schematic example can be seen in Fig. 1(c). All the processes of beam plasma interaction in 3D geometry and the beam attenuation, of major interest for the i-HIBP, are modeled with a dedicated suite of numerical tools called i-HIBPsim. In this work, we aim to present the characterization of the optical system and the validation of the synthetic model. To this end, in the Section II, a

[a)] Corresponding author: poyola@us.es

[b)] See author list of H. Zohm *et al.*, Nucl. Fusion (2024)

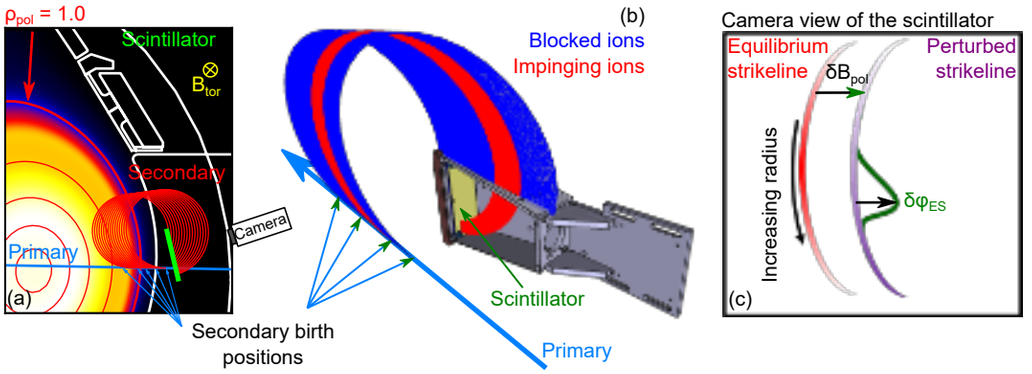

FIG. 1. Working principle of the imaging heavy ion beam probe. (a) Neutral alkali atoms are injected into the plasma where they are ionized and form a secondary fan (red lines). (b) Orbits of a fan of secondary ions are simulated, where the red orbits reach the scintillator, versus those striking the optical support head, which are shown in blue. (c) Expected signal footprint on the scintillator. Changes in the electromagnetic fields cause a change in the orbits trajectory leading to global ($\delta B_{\rm pol}$) and local ($\delta\phi_{\rm ES}$) deviations. Changes in the density modify the intensity pattern.

thorough description of the model is provided, describing the simulation framework and the optical calibration. Then, first measurements are shown in Section III and compared to the synthetic measurements assessing the most important features in the signal, such as the absolute magnitude, signal shape and location on the scintillator.

II. DESCRIPTION OF THE SYNTHETIC MODEL

In this work we present the development of the synthetic model, *i-HIBPsim* code[14], to create synthetic measurement signals, i.e., camera frames, for the i-HIBP diagnostic. The code has been extended to include new physical features and compare against real measurements. The synthetic diagnostic takes as inputs the magnetic field topology, the beam geometry and density and temperature profiles. The synthetic framework first performs the orbit simulation, generating the striking points on the scintillator, along with the corresponding attenuated ion flux. A second part of the framework includes the optical modeling of the system, finally generating the synthetic camera images.

A. Diagnostic geometry

The AUG i-HIBP is installed in the 13th sector of the tokamak. In Fig. 1(a), we present the poloidal view of the injection, indicating the most relevant parameters of the beam, and a 3D view of the optical support, where the scintillator is located, in as shown in (b). The beam is injected 2.7 cm above the midplane, with toroidal and poloidal tilting angles, β and θ, respectively. The β angle is defined by measuring the angle between the radial direction and the beam injection line on the horizontal plane. The radial direction is here constructed by connecting the center of the beam at the injection point on the vessel to the tokamak axis. The Θ angle is defined by the angle that the beam forms with respect to a $z =$ constant plane. The β angle was adjusted during the experimental campaign to modify the location where the particles impinge on the scintillator. The poloidal tilting angle refers to the deflection of the beam with respect to the midplane, and it was found to be in the range $\sim 0.7-1.0^{\rm o}$, slightly deviated from its design value, which is $0^{\rm o}$. The initial geometry of the beam is determined by means of a cross laser emulating the primary beam location after every experimental campaign. This process involves positioning a laser at the source location and aligning it along the beam line. During the experimental campaign, changes in the toroidal injection angle, β, were introduced by mechanically tilting the orientation of the beam line to study changes in the signal.

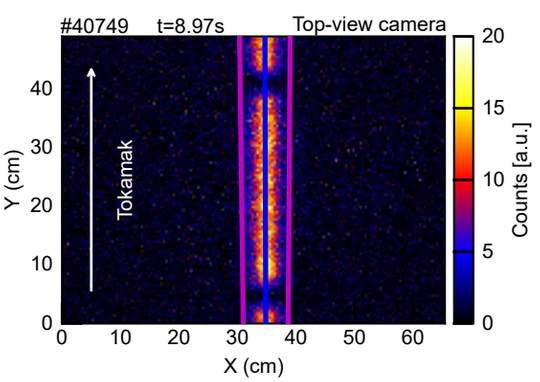

FIG. 2. Beam image from the top beam diagnostic camera (#40749 at $t = 8.9$ s). The image shows the beam, emitting light due to the interaction with the background gas. From the image, the central injection line and the divergence of the beam can be estimated. The beam divergence is estimated from the evolving width of the beam, indicated by the magenta lines, around the central injection line.

Along the beam line, two visible cameras have been installed to determine the beam properties before its

injection into the plasma. In Fig. 2 an experimental image taken from the top-view beam diagnostic camera installed in the beamline, providing the shape and diameter of the neutral beam before it enters the diameter reducer (collimator barrel). It can be seen that the beam has a width of $\sim 7\,\mathrm{mm}$, before collimation. The magenta lines indicate the full width at half-maximum of the signal along the X-direction, and are used to determine the beam divergence with values in the range of $\alpha_{\mathrm{div}} \approx 0.2-0.5^{\mathrm{o}}$. The beam divergence has been found to depend on the choice of the extraction parameters, i.e., the beam optics, and the magnetic field that the coils and the plasma introduce into the beam line. This magnetic field is also the cause of jitters in the beam injection angles, mostly during the ramp-up and ramp-down phases of the discharge.

The final component of the diagnostic geometry is the optical head, where the scintillator is installed. The scintillator head geometry can be seen in Fig. 1(b) with full details, including some exemplary orbits illustrating the diagnostic concept.

B. Beam trajectory simulation

The simulation starts from an input magnetic configuration, typically an axisymmetric plasma equilibrium from the magnetic reconstruction in the ASDEX Upgrade tokamak. The neutral primary beam particles are modeled using straight lines starting at the injection port with the direction given by injection angles, β and Θ. The description of the beam can be modeled with three levels of realism, with increasing computational cost:

1. **Thin-beam approximation**, in which all the beam is concentrated on an infinitesimally thin line following the beam geometry. This mode is typically used for fast calculations and signal level estimations.

2. **Finite-width straight beam**, in which the beam is modeled as a cylindrical beam, aligned along the beam direction. In this situation, all the particles are launched along the same direction, indicated by the injection vector, $\hat{u}$, as schematically presented in Fig. 3.

3. **Finite width with divergent beam**, where the finite-width beam model is complemented by allowing the beam to spread in the velocity direction, accounting for the divergence.

The thin-beam approximation provides significant insight on where the particles are expected and the signal levels. The inclusion of the 3D features of the beam is important to fully reproduce the experimental signal as part of the beam may intercept the 3D structures before reaching the scintillator, as later discussed in Section III. The primary beam is sampled into markers, at the entrance port. These markers are then tracked into the plasma, computing their attenuation, becoming the secondary ionization points. The sampling is done as follows:

- along the primary beam line direction, where markers are sampled equidistantly, allowing to establish a map between initial beam coordinate along the beam direction and the final striking position on the scintillator.

- A Monte-Carlo (MC) based method is used to sample the finite width and divergence. The initial beam is initiated at the injection port, with circular shape, whose radius is taken from the diagnostic camera, shown in Fig. 2. The beam geometry is shown in Fig. 3. This initial circular beam cross-section is uniformly sampled. For the divergence two further degrees of freedom are introduced to describe the vector direction: assuming a Z-axis along the beam direction and centered at the injection port; the azimuthal angle is sampled using a uniform distribution $\xi \sim \mathcal{U}[0, 2\pi)$. The equivalent zenith angle is sampled using a Gaussian distribution centered at 0^{o} with a width of α_{div}, i.e., $\zeta \sim \mathcal{G}(\mu = 0, \sigma = \alpha_{\mathrm{div}})$.

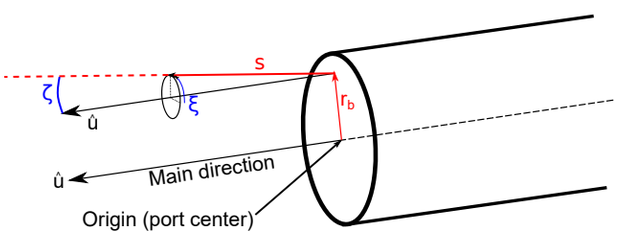

FIG. 3. Coordinate system used in the i-HIBPsim code, to sample the initial markers.

The MC sampling heavily increases the computational cost of the problem, for a reasonable signal quality in the synthetic camera images. To reduce the computing time, the program has been parallelized in the MC sector using MPI[15], allowing for real images to be created within minutes. As the primary beam travels through the plasma, it will suffer from ionization, evolving from its initial neutral state to singly ionized particles. Once ionized, the markers are tracked within the electromagnetic field, which can be provided as either a 2D or 3D input, using a Boris leap-frog algorithm[16], until they reach the scintillator plate. The code now includes a realistic 3D model of the scintillator plate and a CAD model of the enclosing optical head, that is shown in Fig. 1(b), along with some example orbits. As the markers are evolved in the magnetic field, ray-triangle algorithm[17] evaluates collisions with the scintillator plate and also the 3D model of the optical head. To reduce the computational cost of the ray-triangle collision algorithm, a simple octree is performed at the beginning of the code: the code selects a small box fully containing

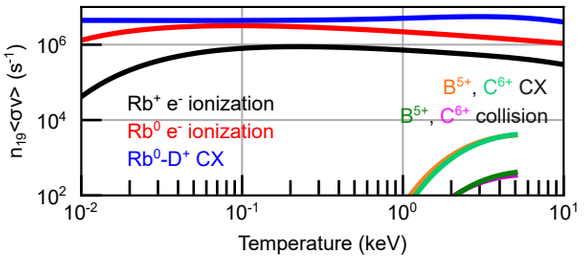

FIG. 4. Reaction rates of the modeled reactions. For the primary beam, the electron impact and charge-exchange (CX) reactions are considered, in red and black, respectively. For the secondary beam, only the electron impact is considered, as the impurity-ionization (with boron and carbon) show negligible reaction rates in comparison. All reaction rates are computed for a beam energy of $E = 70\,\mathrm{keV}$.

the optical head and the scintillator plate, such that only when the advanced positions of the markers are within this box, the ray-triangle collision is checked.

The evolution of the markers weight is given by the beam-attenuation model[3]. The processes taken into account depend on the ionization status:

- The primary beam, this is the neutral beam, is ionized mainly via two physical phenomena: electron impact ionization[18] and charge-exchange reactions[19,20], the latter being the most significant contribution.

- The secondary beam, this is the singly ionized beam fan, ionizes mostly via electron impact ionization[21,22].

Other processes such as collisions with impurities are neglected. The main impurities in the AUG tokamak are carbon and boron, both of which exist at low concentrations within the main plasma $c(B), c(C) \lesssim 1\,\%$, with respect to the main ion density[23]. The cross section of interaction with the boron and carbon can be estimated using tabulated atomic data and corresponding lithium cross sections[24]. In Fig. 4, the reaction rates for the rubidium beam with an energy of $E = 70\,\mathrm{keV}$ are presented. It can be readily seen that the estimated reaction rates for the impurities lie several orders of magnitude below the electron ionization and the main-ion charge-exchange reactions. Thus they will be disregarded in the modeling. Similarly, the neutral density[25] at the edge of the AUG plasmas is of the order of $10^{16}\ \mathrm{m}^{-3}$, that allows also neglecting the contribution of the reaction $\mathrm{D}^0 + \mathrm{Rb}^+ \rightarrow \mathrm{D}^+ + \mathrm{Rb}^0$ for the attenuation of the secondary beam.

C. Optical modeling and calibration

The optical system of the i-HIBP, described in references[3,26], is composed of a set of lenses that collects the light emitted by the scintillator and focuses it into an in-vessel fiber bundle. This fiber bundle connects the optical head to the outside of the vessel. The light is finally collected by a CCD camera, located out-vessel. A complete sketch of the optical system and the contribution to the optical calibration is shown in Fig. 5. To build up actual synthetic images, i.e., camera frames given in pixels and counts per pixel, that can be compared to the experimental measurements, modeling of the optics is implemented as a post-processing of the marker simulation. The optical model for the distortion is determined by a collection of parameters that are calibrated before the campaign: magnification ($\mathcal{D}$), optical axis center and orientation ($x_{\mathrm{center}}, y_{\mathrm{center}}, \alpha$) and optical distortion parameters, both the center of distortion and the distortion scale, ($x_{\mathrm{dist}}, y_{\mathrm{dist}}, k$). For the distortion calibration, during the pre-campaign 2021 calibration at the ASDEX Upgrade tokamak, we used a regular grid pattern at the scintillator plate and recorded it using the optical system. Using the distortion parametrization[27]:

$$\mathcal{D} r_{\mathrm{real}} = \frac{r}{1 + k r^2}, \tag{1}$$

where r is the radial distance from the optical axis in the distorted image; r_{real} is real distance in the pattern; k is the distortion parameter in the model; and $\mathcal{D}$ is the magnification factor, translating from distances in cm to pixels. From the image of a regular pattern in the scintillator, a pre-campaign calibration parameter of $k = 1.7 \cdot 10^{-6}\ \mathrm{pix}^{-2}$ is obtained. However, due to changes in the camera used and slight movements of the optical system, natural from harsh environments like tokamaks, this calibration parameter slightly changed during the experimental campaign. The variations in this distortion only amount up to changes of $\sim 5\%$. This calibration can be tuned during the campaign, since we can get images of the system and use the scintillator outline to determine small shifts with respect to the original calibration. Similarly, calibration of the rest of the parameters can be done on a discharge to discharge basis, to accommodate small shifts of the image. The markers are mapped from their scintillator coordinates in real space (measured in cm) $(x_{\mathrm{real}}, y_{\mathrm{real}})$ into distorted space $(x_{\mathrm{image}}, y_{\mathrm{image}})$ given in pixels, using the corresponding calibration. Representing the markers weight as an histogram in the image space, the synthetic image can be finally obtained. The absolute signal levels are obtained from these images applying the absolute calibration, this is, using the calibrating parameters transforming the ion flux reaching the scintillator into the camera counts.

The total counts per pixel, $C_{\Delta t}$, reaching the scintillator for a given ion flux, ϕ_{ion}, within a given exposure time, Δt, into a camera pixel can be written as:

$$\mathrm{C}_{\Delta t} = \phi_{\mathrm{ion}} \cdot \Upsilon(E) \cdot \frac{\Delta\Omega}{2\pi} \cdot T_{\mathrm{opt}} \cdot \varepsilon_{\mathrm{spec}} \cdot \varepsilon_{\mathrm{geom}} \cdot C_\gamma^{-1} \cdot \Delta t_{\mathrm{exp.}}. \tag{2}$$

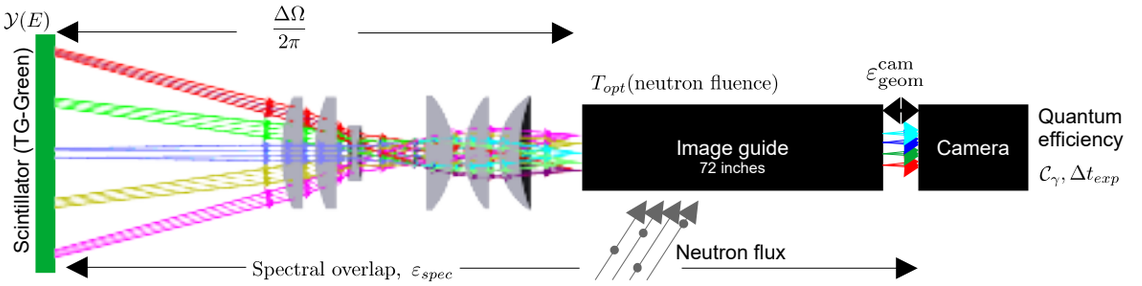

FIG. 5. Optical system scheme, outlining the main contributions to the optical absolute calbration: the scintillation yield, the geometrical apertures at the scintillator side and the camera side, and the fiber bundle, which contributes with a time-varying transmission factor, as it is degraded by the neutron flux.

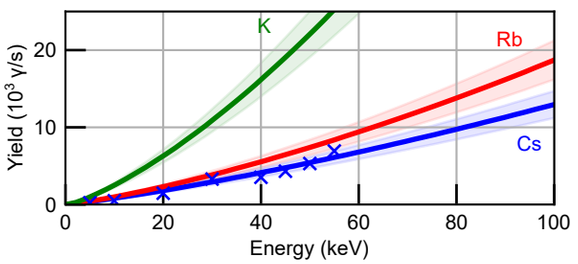

FIG. 6. Yield estimation for the TG-Green scintillator material for rubidium (red) and potassium (green) species. Blue crosses represent the experimental measurements for cesium, and in blue the resulting Birk's law fitting function, along with the 1σ uncertainty estimation in shaded area.

Here $\Upsilon(E)$ is the rate of photons emitted per impinging ion, i.e., the scintillator yield. $\Delta\Omega$ is the solid angle subtended by each pixel into the scintillator while $\varepsilon_{\text{geom}}$ is the geometrical efficiency of each of the pixels of the camera, when observing an optical fiber. $\varepsilon_{\text{spec}}$ represents the spectral overlap of the TG-Green spectra and all the optical components, including lenses, fiber bundle and the camera spectral response. T_{opt} is related to the optical transmission of the fiber bundle, since it degrades throughout the campaign due to the action of the neutron flux[28]. C_γ is the needed number of photons to generate 1 count, following the camera specifications. In Fig. 5, a scheme of the optical setup is shown, indicating the source of each term involved in the absolute calibration. The factors contributing to $C_{\Delta t}$ are described in more detail in the following.

Scintillator yield, $\Upsilon(E)$

The experimental value (which depends on the particle species and energy) has not been measured yet for the rubidium impinging on the TG-Green scintillator. However, an estimate of the actual scintillation yield can be obtained using Birk law[29]. The values of the parameters in the Birk model have been estimated using the experimentally measured yield for cesium[13]. For the Birk model the range and stopping power have been computed with the SRIM package[30,31], using the TG-Green composition[13]. These values can be used to estimate the value of the rubidium and potassium yields for the energy range of interest, assuming that these do not vary among species. The results are presented in Fig. 6, where the experimental yield (cesium), the fitted (blue), the rubidium (red) and potassium (green) estimations are presented. Notice that those are just estimates for the rubidium and potassium, hence only the orders of magnitude are considered to allow for an estimation of the final signal. The typical range of the scintillation yield is around $\sim 1.0 \cdot 10^4 - 1.2 \cdot 10^4$ γ/ion, for the energies of interest for the rubidium. It is also interesting to observe the trend to larger yields by radiation with lighter alkali, which may suggest a better signal-to-noise ratio for those. Future experiments are expected to provide experimental values.

Geometrical efficiency, $\Delta\Omega$

The geometrical efficiency is taken into account in two terms: the first term, explicitly including solid angles, $\Delta\Omega/2\pi$, refers to the geometrical efficiency of collecting the light at the scintillator end of the fiber bundle. The optical modeling of the system provides a numerical aperture, NA = 0.015, which translates into $\Delta\Omega/2\pi = \text{NA}^2/2 = 1.12 \cdot 10^{-4}$.

On the other half of the optical system, going from the optical fiber end towards the camera, a certain geometrical angle is also involved. Between the camera and the image guide, there is a convergent lens installed with focal length of $f = 15\,\text{mm}$ and a lense aperture size of $p = 7\,\text{mm}$. The calculation of the corresponding geometrical efficiency, $\varepsilon_{\text{geom}}$ in the formula (2), is done based on the fiber bundle numerical aperture, provided by the manufacturer NA = 0.604, the pixel size of the camera, labeled as $w = 3.69\,\mu\text{m}$, and the lengths between fiber, lens and the camera, being the latter about 40 mm. Taking into account all the relevant parameters, the geometrical factor is computed to be approximately $\varepsilon_{\text{geom}} \approx 2.4 \cdot 10^{-7}$.

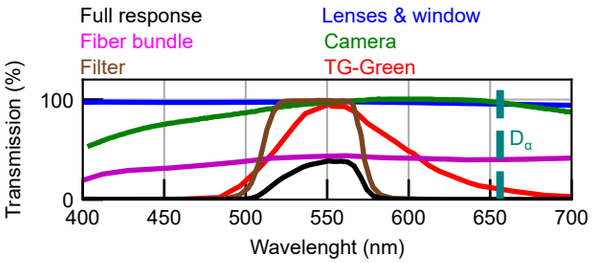

FIG. 7. Spectral response for each of the elements in the optical system. The full response is computed from the product of all the terms. Here, the green dicroic filter is included for the overlap. D_α emission line is included as reference of the most typical background plasma contribution.

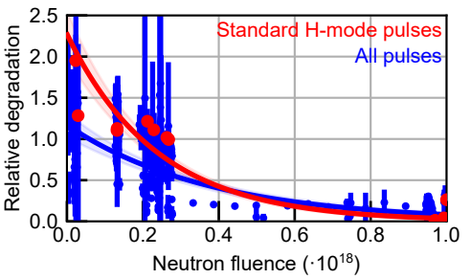

FIG. 8. Fiber bundle degradation factor evolution through the campaign assessed as the ratio between the i-HIBP signals relative to another visible camera viewing the same sector. Points and error bars represent the average are taken from the videos. The red dots correspond to a standard H-mode discharge program, typically carried out in AUG at the beginning of the operation day. This discharge program provides a quasi-reproducible plasma state. The blue points correspond to all the available and useful discharges. Red and blue solid lines represent the fit to the corresponding dataset, and the shaded area their uncertainty.

Spectral overlap

The spectral overlap, $\varepsilon_{\text{spectral}}$, determines the transmission of the light through the optical system, taking into account the wavelength-dependent transmission of each of the components. In Fig. 7, we present the spectral transmission of the lenses, the vacuum window, the fiber bundle along with the TG-Green emission and cameras spectral response. Due to the large visible background light that reaches from the plasma, a dicroic green filter was also installed from the discharges starting with discharge #39860. The spectral transmission of the filter is also included in Fig. 6 for completeness. A value of $\varepsilon_{\text{spectral}} = 22$ % can be reported when using the dicroic filter.

The complete transmission of the optical fiber bundle is estimated from an in-vessel calibration prior to the experimental campaign. The initial value of the transmission is $T_{\text{opt}} = 43\%$, but due to the neutron damage during the campaign, the transmission fast drops down[26] to $\sim 1\%$. To have a quantitative estimate of the degradation, we monitored the camera signal from the background light emitted by the plasma and tracked its evolution through the campaign. Since the light emitted in different plasma situations vary significantly (even for the same discharge scenario), we used a visible light camera viewing the i-HIBP optical head inside the vessel, dubbed 10Cor, for cross-calibration. Synchronized time traces for both the i-HIBP and the 10Cor camera are obtained for up to 300 discharges, removing from this list of pulses in which: no data is available in either camera; there was a change in camera settings; or during ramp-up, ramp-down and ELMy phases. Only discharges with an optical filter installed are considered. The ratio i-HIBP-to-10Cor is computed for each discharge and time point. As we consider the neutron damage as the main responsible for the fiber bundle degradation, the variations in the ratio will be considered as a function of the neutron fluence. In Fig. 8, the degradation ratio is reported as a function of the total neutron flux. In red, we highlight the calculation for the discharges with the standard H-mode scenario, used in AUG for the beginning of each shot day. It is clear that there is consistent degradation of the fiber as a function of the neutron flux. We assume the following functional form:

$$\mathrm{T}_{\text{opt}} = \mathrm{T}_0 \cdot \mathrm{e}^{-\phi_n/\tau_n}, \tag{3}$$

where T_0 is the transmission scale, ϕ_n is the neutron fluence and τ_n is the half-life of the transmission. From the fitting process of the data in Fig. 8, the half-life has been estimated as $\tau_n = (3.8 \pm 0.5) \cdot 10^{17}$ neutrons. This value is roughly consistent with the observed degradation of the fiber in the previous campaign, when it degraded down to < 1 % after the full campaign irradiation, which matches with a gross estimation of $\tau_n \sim 9 \cdot 10^{17}$ neutrons. The value obtained from the standard H-mode discharges (red in the Fig. 8) is consistent with a degradation of $\tau_n = (2.4 \pm 0.6) \cdot 10^{17}$ neutrons

In the campaign 21/22 an in-situ in-vessel system was installed along with the fiber bundle allowing to bake it and partially recover the transmission. It is firstly used after discharge #40303, where up to a 10% transmission was recovered[26]. Ex-vessel heating recovery was able to heal the transmission, after a day, up to 40%, almost its original transmission value.

III. FIRST SIGNALS AND COMPARISON WITH SYNTHETIC SIGNALS

During the experimental campaign 2021–2022 first signals were obtained from the i-HIBP diagnostic[26], using rubidium as the probing ion. The availability of first signals, enables the validation of the synthetic model, *i-HIBPsim*: from the reactivities of the different reactions, to the validity of the optical calibrations and the shape and signal levels observed during the plasma pulses. This section will be divided into two parts: first, we will describe the validation of the synthetic model only comparing the shape and location of the scintillator light

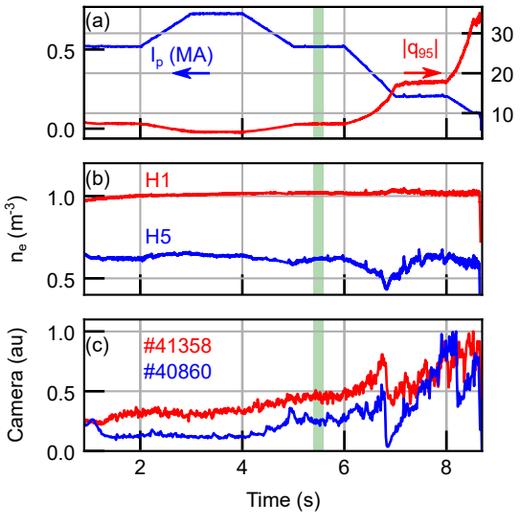

FIG. 9. Timetraces of the AUG plasma pulses #40860 and #41358, which were run with the same discharge program, with a magnetic field at the axis of $B_t^{\text{axis}} = -2.5\,\text{T}$. In (a), the plasma current timetrace is depicted in blue, and the q_{95} in red, as provided by the magnetic reconstruction in the EQH diagnostic. For both discharges, the current steps were the same and (so the same q_{95}). (b) Line-averaged densities from the DCN interferometer are presented. H1 (in red) is one of the chords integrating through the core, while H5 (in blue) is integrating along mostly through the pedestal. H1 and H5 are similar in both discharges, so a single pair is here presented for clarity. (c) Timetraces of the camera signal, after applying noise subtraction was applied are shown in both cases.

pattern with respect to their respective experimental counterparts; and a second part, where we provide a detailed comparison of the signal levels.

A. Validation of shape and location

To demonstrate the quality of the synthetic modeling and the calibrations performed in the previous section, two plasma pulses are considered for this validation: #40860 and #41358, as two different toroidal injection angles, $\beta = 4.0^{\text{o}}$ and $\beta = 4.7^{\text{o}}$, were tested. Verification in the two extreme values of the injection angle against the experimental measurements is advantageous, as the location of the light pattern on the scintillator is quite sensitive to β. These plasma pulses were designed as low-density L-modes to minimize the background light and obtain sufficiently high signal levels were obtained to compare the features in the image. For reference, in Fig. 9, the time traces of main plasma parameters for the two discharges are provided: the plasma current and edge safety factor q_{95} value (the magnetic field fixed to $-2.5\,\text{T}$ at the magnetic axis in both cases) in Fig. 9(a), the line-averaged plasma density along two chords, going through the plasma core and edge in Fig. 9(b), and the time traces of the integrated camera signals in Fig. 9(c). In the two discharges, the magnetic topology is changed by varying in long steps the plasma current ranging from $I_\text{p} = 0.2\,\text{MA}$ up to $I_\text{p} = 0.75\,\text{MA}$. Both discharges are run following the same discharge program, leading to similar time traces of the current and the line-averaged densities, H1 (core chord) and H5 (edge chord) presented in Fig. 9(a,b). For clarity, only the traces of one of the discharges is presented in those figures. In each of the current steps, signals were obtained as it is depicted in Fig. 9(c). The time traces presented there were obtained by subtracting the light noise from the plasma from the total camera signal, thus they only contain information on the scintillator emission.

We run the synthetic model using the finite beam width model for these particular plasma scenarios in the time shown in the green shaded area, with and without including the full 3D model of the optical head. The corresponding results are shown in Fig. 10. In Fig. 10(a,b) we show the experimental measurements, evaluated at $t = 5.5$ s for both cases, where we have the largest current in the plasma ($\text{I}_\text{p} = 0.75$ MA) in the scenario. To ease the visualization, a time window $\Delta t_{\text{window}} = 200\,\text{ms}$ is integrated around the central time. We see that for the lowest injection angle, i.e., the discharge #40860, the experimental signal features a hard cut-off in the signal on the leftmost side of the image, which is indicated by the white-dashed line. This hard cut-off, however, is not observed on the signal in #41358, as shown in (b). When the simulation is done only with the scintillator plate, without the 3D model of the head, the hard cut-off observed in #40860, cannot be reproduced, as shown in Fig. 10(c). In the second discharge, #41358, where the injector beam was further tilted away from the radial direction, neither the signal nor the synthetic image are affected by this cut-off, even without the 3D model of the head, as shown in Fig. 10(c). Whenever, the 3D model is included in the simulation, its blocking action (shown in Fig. 10(e)) allows the cut-off feature to be numerically reproduced. This demonstrates two main features:

- the 3D model of the head is required to fully reproduce and interpret the signals observed in experiments;
- the cut-off can be avoided when increasing the toroidal injection angle β.

The cut-off in the Fig. 10(a,e) was computed directly from the synthetic signal and over plotted in both images. This, again, demonstrates the good match between the synthetic model and the experiment.

B. Comparison of the absolute signal levels

The comparison of the absolute signals for the i-HIBP diagnostic features a challenge: the uncertainties in the scintillator yield and the optical transmission degradation due to the neutron damage make the

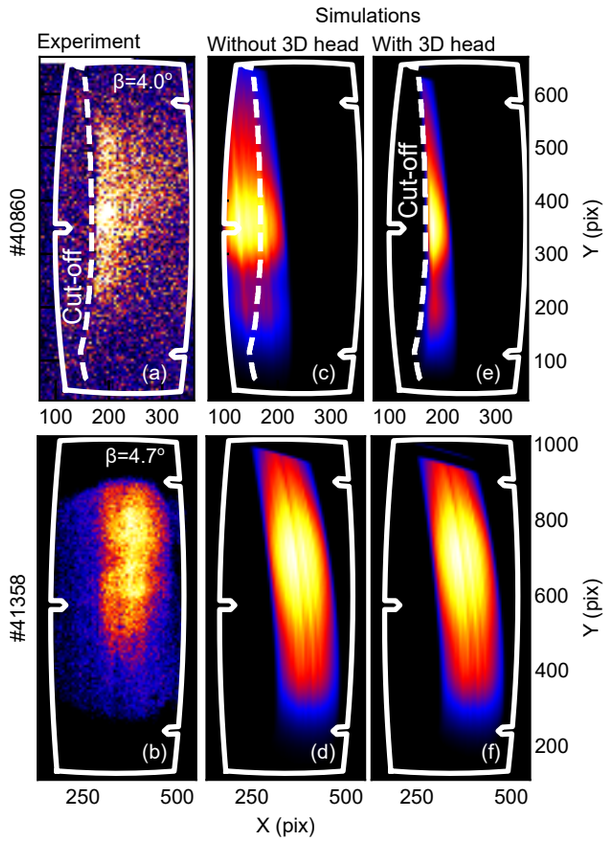

FIG. 10. Comparison between the measured camera frames and the synthetic camera frames obtained with i-HIBPsim. The upper row (a, c, e) figures are related to #40860 at $t = 5\,5s$, while the second row (b, d, f) are the ones related to the #40860 at $t = 5.5\,\mathrm{s}$. The first column contains the measured camera frames with white lines indicating the scintillator border. The second column is the synthetic image generated without the 3D model of the detector head (only the scintillator), while the last column includes it.

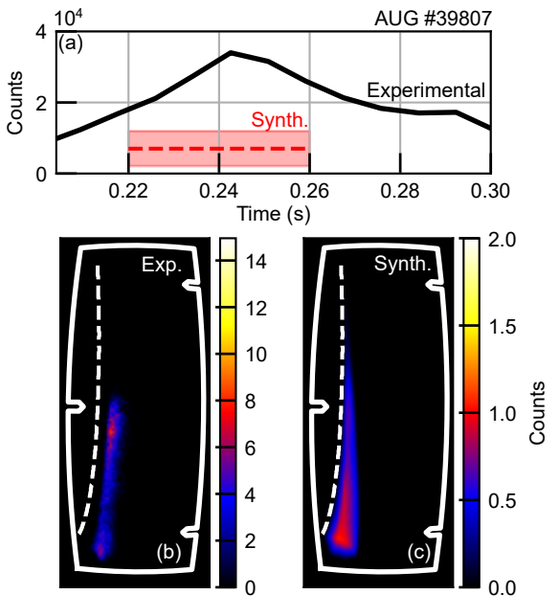

FIG. 11. Quantitative intensity comparison.(a) Timetrace with the total count from the camera signal, integrated within the scintillator region (black). In red, the corresponding integrated synthetic signal on the scintillator, taking into account the absolute calibration.The 2D intensity pattern of (b) and the synthetic frame (c) are presented. The red band in (a) is the estimated error band, assuming a conservative level of uncertainties in the optical calibration parameters and a 20% uncertainty in the global density value.

estimate rather inaccurate. However, orders of magnitude are useful to validate the diagnostic and the synthetic model, being able to project further improvements and design the optimal measurement scenarios. We take for the signal estimation the plasma discharge #39807 where no signals of strong degradation are observed and a high enough signal is observed. In that experiment, the optical filter was not installed, hence a larger background noise is expected. We are using the signal obtained during the plasma current ramp-up phase of the discharge, because the background light from the plasma does not allow for measurements during the flat top phase. In Fig. 11(a), we show the time traces of the signal in the time range $t \in (200, 300)$ ms. The time trace was obtained after applying background subtraction to the raw signal from the camera. A full 3D simulation was conducted using the magnetic reconstruction from the CLISTE[32] code, for the time point $t = 0.253\,\mathrm{s}$ of the discharge #39807. The density and temperature profiles were fitted to the Thomson scattering and DCN interferometer data using a modified hyperbolic tangent[33]. From the synthetic signal we can estimate the actual camera count signal expected in the experiment by means of equation (2). In this Fig. 11(a), the estimated value is shown in red, along with a shaded area, indicating the uncertainties assumed before. Although the synthetic frame count is a factor of about 10 lower than the experimental signal level, still be considered qualitatively a good agreement, considering the aforementioned uncertainties and those coming from the density and temperature estimations. Up to a 6-fold disagreement has also been reported in other diagnostics as the AUG tokamak using the TG-Green material[34], and, thus, similar levels are here expected. It is noticeable that small variations of the electron density at the edge, may significantly impact the final signal[26]. Following the beam attenuation model, the attenuation exponentially grows with the density $\Delta I_{\mathrm{beam}} \propto \exp(-n_e)$. A global uncertainty in the density of 20 %, translates into a signal variation of approximately 30 %. However, this is a desired feature of the diagnostic, as it will allow for precise density measurements, that can go beyond the current diagnostics at the plasma edge. It is also important to characterize the maximum signal levels expected and compare to those of the signals. The maximum signal levels would allow us to estimate whether a given scenario is measurable. In the same case, the maximum signal

corresponds to a count in the experimental camera of $C_{\text{exp}} = 4$ counts while from the synthetic diagnostic and the calibration, the maximum synthetic value is $C_{\text{synth}} = 1 \pm 0.7$ counts. The reconstructed and experimental frames are shown in Fig. 11(b,c), respectively. The mismatch in the actual location of the cut-off (indicated by the white dashed line) computed from the synthetic image is expected, as during the ramp-up phase, the beam suffers from small jitters in the beam line, which were not included in the modeling for this comparison.

IV. DISCUSSION AND OUTLOOK

First measurements of the imaging heavy ion beam probe have been thoroughly analyzed and studied with the numerical model suite i-HIBPsim. The completeness of the model allows the reproduction of relevant physical features, in a computationally efficient way, such as the shadowing from the scintillator head and the signal shape and location. The absolute calibration of the system, albeit the experimental uncertainties in both the fiber bundle and the scintillator yield, match within reasonable agreement with the experimental signal levels. This matching of the signal levels allows predictive calculations to be performed to improve the transmission of the system, such a choosing a lighter element like potassium, with a lower secondary ionization reaction rate and higher scintillation yield. The potassium is one of the candidates for future campaigns, as higher scintillation yields are expected, and lower beam attenuation due to its lower mass. The synthetic model has shown a good level of matching on the shape and signal levels, as demonstrated in the cut-off feature and in the shape of the synthetic frames, compared to camera images. It has also been shown that the synthetic diagnostic i-HIBPsim is a good tool to not only reproduce the signals, but also to interpret the underlying physics.

ACKNOWLEDGMENTS

This work received funding from the Spanish Ministry of Science under Grant No. FPU19/02267. G. Birkenmeier acknowledges the Helmholtz Association under Grant No. VH-NG-1350 for the support. E. Viezzer acknowledges the European Research Council (ERC) under the European Union's Horizon 2020 research and innovation program Grant No. 805162 for the support. J. Galdon-Quiroga acknowledges the support of the European Union under Marie Sklodowska Curie Grant Agreement No. 101069021.

DATA AVAILABILITY

The data that support the findings of this study are available from the corresponding author upon reasonable request.

REFERENCES

[1]E. Viezzer *et al.*, Nuclear Materials and Energy **34**, 101308 (2023).
[2]J. Galdon-Quiroga *et al.*, Journal of Instrumentation **12** (2017), 10.1088/1748-0221/12/08/C08023.
[3]G. Birkenmeier *et al.*, 45th EPS Conference on Plasma Physics, EPS 2018 **2018-July**, 1032–1035 (2018).
[4]G. Anda *et al.*, Review of Scientific Instruments **89**, 013503 (2018).
[5]G. Birkenmeier *et al.*, Journal of Instrumentation **14**, C10030–C10030 (2019).
[6]G. Birkenmeier *et al.*, Fusion Engineering and Design **168**, 112644 (2021).
[7]P. M. Schoch *et al.*, Review of Scientific Instruments **59**, 1646–1651 (1988).
[8]T. P. Crowley, IEEE Transactions on Plasma Science **22**, 291–309 (1994).
[9]A. V. Melnikov *et al.*, Nuclear Fusion **57**, 072004 (2017).
[10]R. Jiménez-Gómez *et al.*, Nuclear Fusion **51**, 033001 (2011).
[11]A. Fujisawa *et al.*, Physical Review Letters **93**, 165002 (2004).
[12]T. Ido *et al.*, Physical Review Letters **88**, 055006 (2002).
[13]J. J. Toledo-Garrido *et al.*, Journal of Instrumentation **17**, P02026 (2022).
[14]P. Oyola *et al.*, Review of Scientific Instruments **92** (2021), 10.1063/5.0043757.
[15]Message Passing Interface Forum, *MPI: A Message-Passing Interface Standard Version 4.1* (2023).
[16]J. P. Boris, Proceedings of the Fourth Conference on Numerical Simulation of Plasmas , 3–67 (1971).
[17]T. Möller and B. Trumbore, Journal of Graphic Tools **2**, 21–28 (1997).
[18]W. Lotz, The Astrophysical Journal Supplement Series **14**, 207 (1967).
[19]F. Ebel and E. Salzborn, Journal of Physics B: Atomic and Molecular Physics **20**, 4531 (1987).
[20]R. J. Girnius *et al.*, Nuclear Instruments and Methods **143**, 505–511 (1977).
[21]M. J. Higgins *et al.*, "Technical report clm-r294," Tech. Rep. (Culham Laboratory, 1989).
[22]D. W. Hughes and R. K. Feeney, Physical Review A **23**, 2241 (1981).
[23]F. Ryter *et al.*, Nuclear Fusion **53**, 113003 (2013).
[24]D. Wutte *et al.*, Atomic Data and Nuclear Data Tables **65**, 155–180 (1997).
[25]A. Jansen van Vuuren *et al.*, Nuclear Fusion **61**, 046001 (2021).
[26]J. Galdon-Quiroga *et al.*, Review of Scientific Instruments **95** (2024), 10.1063/5.0175720.
[27]F. Bukhari and M. N. Dailey, Journal of Mathematical Imaging and Vision **45**, 31–45 (2013).
[28]S. Rizzolo *et al.*, AIP Conf. Proc. **1624**, 111–117 (2014).
[29]J. B. Birks, Proceedings of the Physical Society. Section A **64**, 874 (1951).
[30]J. F. Ziegler *et al.*, Nuclear Instruments and Methods in Physics Research Section B: Beam Interactions with Materials and Atoms **268**, 1818–1823 (2010).
[31]C. Ostrouchov *et al.*, Journal of Open Source Software **3**, 829 (2018).
[32]P. J. M. Carthy, Physics of Plasmas **6**, 3554–3560 (1999).
[33]P. A. Schneider, Ph.D. thesis.
[34]J. Rueda-Rueda *et al.*, Plasma Physics and Controlled Fusion **66**, 035008 (2024).